Real-time shape estimation of very flexible aircraft structures through complementary filtering

Francisco P. Reis, Leandro R. Lustosa, Charles Poussot-Vassal

Available online at www.sciencedirect.com

ScienceDirect

IFAC Papers Online CONFERENCE PAPER ARCHIVE

IFAC PapersOnLine 56-2 (2023) 10746–10751

Real-time shape estimation of very flexible aircraft structures through complementary filtering

Francisco P. Reis * **Leandro R. Lustosa** *
Charles Poussot-Vassal **

* *ISAE-SUPAERO, Université de Toulouse, France*
(e-mail: {francisco.pedrosa-reis,leandro.lustosa}@isae-supaero.fr)
** *ONERA, Université de Toulouse, France*
(e-mail: charles.poussot-vassal@onera.fr)

Abstract: This paper proposes a method for high-bandwidth, low-latency state estimation of highly-deformed beam-like flexible structures considering piecewise-constant torsion and curvature distributions for active shape control purposes. It does not rely on knowledge of the aircraft's structural and aerodynamic dynamic models in a similar sense that an inertial navigation system does not rely on the flight mechanics model of the aircraft it belongs. The method uses the section extremities attitudes, estimated using complementary filtering, to determine torsion and curvature. Finally, the paper analyzes the estimator's frequency domain properties around chosen equilibrium conditions.

Keywords: Guidance, navigation and control of vehicles, Mechanical and aerospace estimation, Avionics and on-board equipment, Shape control, Complementary filtering, Very flexible aircraft

1. INTRODUCTION

The increased lift-to-drag ratio of highly slender wings provides valuable performance featuresthrough, such as the capacity to fly at higher altitudes and extended endurance. However, these benefits require a light structural design that often couples the vehicles' structural and flight mechanics' dynamic modes. This coupling yields decreased handling qualities or even instabilities that preclude airworthiness. A noteworthy example is the X-HALE demonstrator platform developed at the University of Michigan. Previous work (González et al. (2018)) showed that open-loop piloting of this very flexible aircraft yielded a pilot rating of 9 on the Cooper-Harper Handling Qualities Rating Scale (HQRS), meaning that intense pilot compensation was required to retain control and significant deficiencies were present. After introducing a Stabilization Augmentation System (SAS) based solely on the rigid body mode sensing feedback (i.e., one inertial measurement unit placed at the aircraft center), the Cooper-Harper HQRS rating improved to 4, meaning that desired performance required moderate pilot compensation and showed very objectionable but tolerable deficiencies. The **HALION** Project at ISAE-SUPAERO investigates the possibility of further increasing handling qualities by introducing real-time wing-shape estimators into the SAS loop.

While previous work in the literature focused on Bayesian estimation (Zhang et al. (2022)) or optimization methods (Pang and Cesnik (2016)) that rely on aircraft aeroelastic dynamics models, the **HALION** Project pursues an aircraft-independent formulation. To achieve this objective, previous work (Lustosa et al. (2021)) demonstrated the viability of integrating an array of rate-gyro angular velocities distributed across a wing to obtain high-bandwidth mode shape amplitude estimators with errors that diverged with time. An extended Kalman filter (EKF) incorporated measures from a low-bandwidth computer vision system that tracked active markers on the same wing to bound unstable errors and calibrate rate gyro biases in flight. Although conceptually similar, we recall that standalone texture-based computer vision methods routinely used in test flights today are not real-time in view of very flexible aircraft feedback systems requirements (Meyer et al. (2014); Renaud et al. (2022)). Previous flexible aircraft applications and techniques are discussed in (Lustosa et al. (2021)).

To bound rate gyro integration errors, an alternative to computer vision as an aiding device to the EKF is to employ accelerometers and magnetometers. This bypass the need for energetically expensive computer vision avionics or potentially significant delay margins requirements due to computer vision routines processing in embedded computers. A common strategy in low-cost avionics, often called complementary filtering, is comparing the measured gravitational and magnetic fields to their expected values — as given by the rate gyro standalone solution — and using any divergences to correct the attitude computation. This technique yields almost-global asymptotic convergence for rigid-body attitude estimation with the possibility of rate gyro bias in-flight calibration (Mahony et al. (2008)). While commonplace in the scientific community for rigid body attitude estimation, our present work investigates computational procedures to exploit comple-

10.1016/j.ifacol.2023.10.737

mentary filtering techniques for flexible structure state estimation.

The remainder of the paper is organized as follows. Sec. 2 formulates the problem and recalls a few geometric notions. Sec. 3 derives and proposes a curvature and torsion estimator for a wing undergoing vibration clamped to an inertial frame. Sec. 4 analyses the frequency domain response of the method for wing shape estimation in practice, and Sec. 5 concludes the paper and suggests directions for future work.

2. PROBLEM FORMULATION

2.1 1-Dimensional Beam-like Structural Elements

Similarly to Cesnik and Brown (2003), we model a structural element as a 1-dimensional specialized beam element with only three strain degrees of freedom: torsion, in-plane bending, and out-of-plane bending (neglecting span-wise extension). According to Reis et al. (2022), "The element's neutral axis uses a reference curve to track the structural element shape. A coordinate s determines the position along the reference curve, sweeping from 0 to the beam element length. The plane perpendicular to the curve in the neutral position is assumed to stay perpendicular to the curve independently of the element's deformation." Figure 1 illustrates a reference curve attached to a flexible wing.

Additionally, "from the reference curve, a reference frame is defined as follows: the x-axis aligns with the reference curve on the wing (torsion direction), the y-axis points to the leading edge (out-of-plane bending direction), and the z-axis points to the result of their cross-product (in-plane bending direction)." (Reis et al. (2022))

The assumptions related to the undeformed beam's cross-sections makes the structural element similar to an Euler-Bernoulli beam. Since cross-sections remain plane and perpendicular to the reference curve, sensors installed in a given cross-section are considered to have the same attitude as their intersection with the reference curve. Therefore, off-centered estimated attitudes are indistinguishable from their reference curve counterpart. These assumptions could be forgone to generalize the method, however, this modification would require the inclusion of compensations to the cross-section's deformations.

Furthermore, curvature and torsion along the beam-like element are considered constant, similarly to Cesnik and Brown (2003). The terms curvature (i.e. $\kappa \in \mathbb{R}^+$) and torsion (i.e. $\tau \in \mathbb{R}$) refer to the concepts with the same name from differential geometry. In a Frenet-Serret frame the two values are defined as

$$\boldsymbol{T}' = \kappa \boldsymbol{N} \quad \text{and} \quad \boldsymbol{B}' = -\tau \boldsymbol{N}. \tag{1}$$

Moreover, the projections of $\kappa \boldsymbol{B}$ into axes y and z are referred as κ_y and κ_z, respectively. As per the fundamental theorem of space curves, these two properties (i.e. κ and τ) are sufficient to describe the shape of a space curve.

2.2 Structure Breakdown and Setup

The estimation of the overall wing shape is divided into pre-defined wing sections, where a section is a segment in-

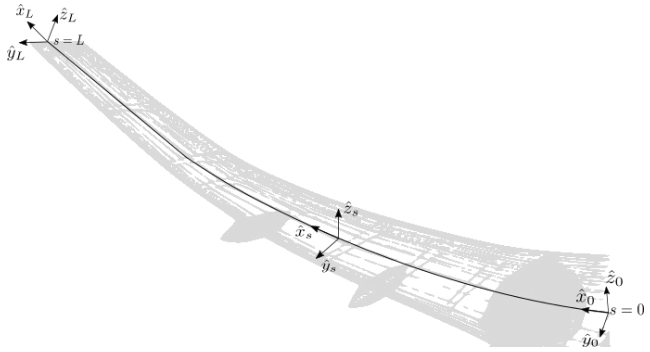

Fig. 1. Reference frames of three points on the reference curve (adapted from Reis et al. (2022)).

between two consecutive fixed stations located at $s = s_i$ and $s = s_{i+1}$. Each section will be considered to be a structural element, as described in Sec. 2.1. Moreover, in this article s_i and s_{i+1} will be considered to be $s = 0$ and $s = L$ (L is the length of the reference curve between the two wing section extremities, ergo $L \in \mathbb{R}^+$). All stations are equipped with Inertial Measurement Units (IMUs) providing rate gyro, magnetometer, and accelerometer measurements. The estimated orientation of each IMU station, referred as $\hat{D}(s,t)$, is available through complementary filtering on SO(3).

2.3 Complementary Filtering

Complementary filtering on $SO(3)$ exploits IMU data to output the attitude of station points in the form of Direction Cosine Matrices (DCM). Our filters are based on the work of Mahony et al. (2008) and, more precisely, implement the *explicit complementary filter with bias correction* formulation. They were tuned to no specific performance target other than the suggested design constraints given in the aforementioned article.

These estimators integrate the rate gyro measurements while simultaneously applying attitude corrections using the accelerometers and magnetometer measurements. This correction carries dynamics, and its effect on the overall wing shape estimator dynamics is studied in Sec. 4. This particular implementation also computes a rate gyro bias estimate for in-flight calibration purposes. However, in this article, the bias estimation term is neglected.

3. CURVATURE CALCULATION DD0T

This section introduces an algorithm capable of estimating the constant curvature of a wing section. It uses the estimated attitudes from the complementary filters and Rodrigues' Rotation Formula,

$$e^{[\boldsymbol{V}\times]} = I_3 + \frac{\sin(\theta)}{\theta}[\boldsymbol{V}\times] + \frac{1-\cos(\theta)}{\theta^2}[\boldsymbol{V}\times]^2 \tag{2}$$

where $\boldsymbol{V} \in \mathbb{R}^3$, θ the Euclidean norm of $\boldsymbol{V}$, and $[\,\cdot\,\times] : \mathbb{R}^3 \to \mathfrak{so}(3)$ is the associated left vector product operator, in the case of $[\boldsymbol{V}\times]$ it is equal to

$$[\boldsymbol{V}\times] = \begin{bmatrix} 0 & -v_3 & v_2 \\ v_3 & 0 & -v_1 \\ -v_2 & v_1 & 0 \end{bmatrix}. \tag{3}$$

For further context, $\mathfrak{so}(3)$ is the set of all skew-symmetric 3×3 matrices. It is also the notation used to designate the

Lie algebra associated with the special orthogonal group denoted $SO(3)$, which is a Lie Group. The inverse of the associated left vector product operator is called vex, where $\text{vex} : \mathfrak{so}(3) \to \mathbb{R}^3$.

3.1 Algorithm Derivation

Following the representation of Reis et al. (2022): "Attitudes along the reference curve will be represented by a deformation map $D(s,t) : \mathbb{R}^2 \to SO(3)$, where $s \in \mathbb{R}$, $t \in \mathbb{R}$, and $D \in SO(3)$ are, respectively, the wing station (continuous) arc length coordinate (see Fig. 1), time instant, and local rotation deformation." This algorithm is based on the local rotation deformation dynamic equation along the reference curve, given by

$$\frac{\partial}{\partial s} D(s,t) = -[\boldsymbol{K}(s,t)\times] D(s,t) \tag{4}$$

where $\boldsymbol{K} \in \mathbb{R}^3$ is the vector containing τ, κ_y, and κ_z. The solution to this equation, when $\boldsymbol{K}$ is constant between two points s and s_0, is

$$D(s,t) = e^{-[\boldsymbol{K}(t)\times](s-s0)} D_0(t) \tag{5}$$

where $D_0(t) = D(s_0,t)$. By multiplying both sides by $D_0^T(t)$ the equation results in

$$e^{-[\boldsymbol{K}(t)\times](s-s0)} = D(s,t) D_0(t)^T. \tag{6}$$

Per Sec. 2.2, the two points used for this analysis are both extremities of the reference curve along the wing section, $s_0 = 0$ and $s = L$. For notation concision, D_0 designates the attitude at $s = 0$ in function of time $D(0,t)$. Similarly, D designates the equivalent at the other extremity, $s = L$, resulting in

$$e^{-[\boldsymbol{K}(t)\times]L} = D D_0^T, \tag{7}$$

which provides the method its name, *DD0T*. Since both D and D_0 can be estimated by the complementary filter, they are considered known values. Therefore only the left side of the equation remains unsolved. A logarithm of the resulting matrix could determine $\boldsymbol{K}(t)$, however, given its required computational cost, this article proposes another method. Using the Rodrigues Rotation Formula presented in (2), the equation becomes

$$D D_0^T = I_3 - \frac{\sin(\alpha L)}{\alpha}[\boldsymbol{K}(t)\times] + \frac{1-\cos(\alpha L)}{\alpha^2}[\boldsymbol{K}(t)\times]^2, \tag{8}$$

where α is the Euclidean norm of $\boldsymbol{K}(t)$. By the definition of $[\boldsymbol{K}(t)\times]$, the second term is always purely asymmetric while the identity matrix and the third term are always symmetric. By isolating the asymmetric part of the left side of the equation and applying the vex operator,

$$\boldsymbol{W} = \text{vex}\left(\frac{D D_0^T - D_0 D^T}{2}\right) = -\frac{\sin(\alpha(t) L)}{\alpha(t)} \boldsymbol{K}(t), \tag{9}$$

where $\boldsymbol{W} \in \mathbb{R}^3$ will be used to simplify the notation. Assuming the sine to be positive and taking the Euclidean norm, the previous equation becomes

$$\|\boldsymbol{W}\| = \sin(\alpha(t) L) \tag{10}$$

since $\alpha = \|\boldsymbol{K}(t)\|$. Calculating the sine inverse $\alpha(t)$ can be calculated by

$$\alpha(t) = \frac{\arcsin(\|\boldsymbol{W}\|)}{L}. \tag{11}$$

By applying (10) and (11) in (9), the equation of $\boldsymbol{K}(t)$ becomes

$$\boldsymbol{K}(t) = -\frac{\arcsin(\|\boldsymbol{W}\|)}{\|\boldsymbol{W}\| L} \boldsymbol{W}. \tag{12}$$

Since $\boldsymbol{W}$ only depends of D and D_0, the equation above can estimate $\hat{\boldsymbol{K}}(t)$ using the estimated values $\hat{D}$ and $\hat{D}_0$ obtained from the complementary filters.

3.2 Special Case

Considering that this method is limited to $0 \leq \alpha(t) L \leq \frac{\pi}{2}$, it only presents one special case whenever $\alpha(t) = 0$. In this case, $\boldsymbol{W}$ and $\boldsymbol{K}$ are both equal to zero, making it easy to identify. Also D and D_0 will be identical.

3.3 Limitations and Improvements

The *DD0T* method in the presented form is limited to $0 \leq \alpha(t) L \leq \frac{\pi}{2}$. By including the symmetric part of $D D_0^T$, the algorithm can be adapted to identify angles in $0 \leq \alpha(t) L \leq \pi$. For the applications foreseen by the authors the implementation using only the asymmetric term is sufficient, but for other application the complete method can be used.

4. FREQUENCY DOMAIN ANALYSIS

This section studies the method's properties in the frequency domain. For that purpose, the *DD0T* estimator proposed has been programmed in a simulator with the architecture depicted in Fig. 2. Structural dynamics are not considered in the model since the estimator only requires kinematics data. Moreover, the analysis exploits the results of the following four tests.

Test 1. $\frac{\hat{\boldsymbol{K}}(t)}{\boldsymbol{K}(t)}$ This test emphasizes the relation between estimated and real curvatures. By introducing an oscillating curvature on one axis between τ, κ_y, and κ_z, the coupling between inputs and outputs can be observed.

Test 2. $\frac{\hat{\boldsymbol{K}}(t)}{\boldsymbol{K}(t)}$ *(Corrective term only.)* Rate gyro measurements are not considered in the test to focus the results on the corrective behaviour of the complementary filter. Similarly to Test 1, the input axes are excited with curvature oscillations. Thus, the coupling between inputs and outputs can be analyzed.

Test 3. $\frac{\hat{\boldsymbol{K}}(t)}{\boldsymbol{K}(t)}$ *(Corrective term only and different tuning.)* To present the effect created by the complementary filter tuning, its performance is contrasted against a different set of gains. Similarly to the previous tests, the input axes are excited with curvature oscillations to allow for a coupling analysis between inputs and outputs can be analyzed.

Test 4. $\frac{\hat{\boldsymbol{K}}(t)-\boldsymbol{K}}{N_i}$ *(Error over noise.)* In this test, for a given stable shape (i.e., constant $\boldsymbol{K}$), noise will be introduced on the rate gyro measurements one axis at a time. The experimental outcome supports analysing the transfer function from gyro noise to estimated outputs.

Results were simulated for a total of sixteen complete cycles for a given frequency, and only the second half of these results were taken for post-treatment to eliminate

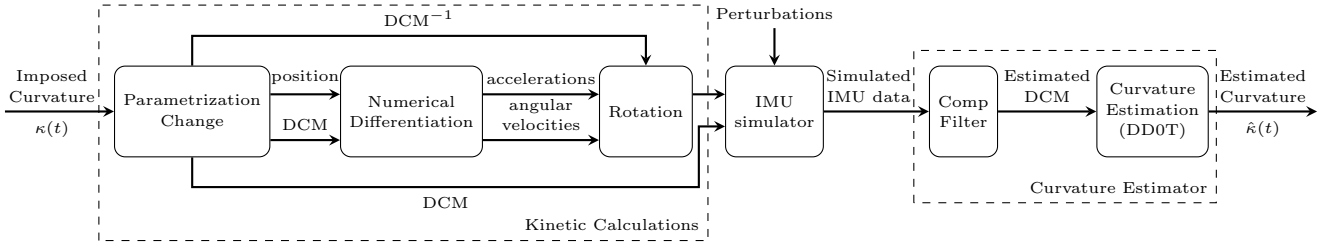

Fig. 2. Flowchart of the simulator architecture, showing calculations done between imposed and estimated curvatures.

any transitory effect. The data treatment methodology consisted of taking the Fourier transform of the remaining output and analysing the signal for magnitude and phase. These values were stored and used to generate the graphs in this section. For certain frequencies, nonlinear behaviour caused the excitation of frequencies other than the input frequency and a bias was identified for longer transitory behaviour.

To eliminate ambiguities between nonlinear or numeric noise cases, any magnitude bigger than one percent of the input frequency magnitude was considered a nonlinear case. For this reason, parts of the graph are not continuous. Also, while the data on the following graphs is discrete, continuous curves are used to facilitate data presentation. Finally, the lower frequencies were limited by computer memory and simulation time, while higher frequencies often present nonlinear behaviour incompatible with linear analysis tools.

4.1 Complete Filter Against its Complementary Part

Figure 3 illustrates the Bode plots outcome for Tests 1 and 2. With both the rate gyro and the complementary terms, the direct terms (e.g., $\hat{\tau}/\tau$, $\hat{\kappa_y}/\kappa_y$, and $\hat{\kappa_z}/\kappa_z$) can follow the input on the three axes with no visible delays on the whole frequency window analyzed. The crossed terms between the different axes (e.g., $\hat{\tau}/\kappa_y$, $\hat{\kappa_z}/\tau$) present steep ascending magnitudes of around $+40dB/decade$ on lower frequencies, with matching phases of around $+180°$. This is a good indication that the system observed presents two slower LHP-zeros before the beginning of the graph and shows some trend of slowing down would mean the presence of some LHP-poles around that zone. The rest of the trend is unavailable due to increased nonlinear events at higher frequencies.

The results show different behavior for the pure complementary parts of the filter. The direct terms match in magnitude up to between 0.1 to $1rad/s$ depending on the axis. A phase shift is also noticeable. For lower frequencies, the crossed terms grow in magnitudes around $+20dB/decade$, indicating the presence of one single zero. In other words, it lacks one of the previously noticed zeros for the complete filter. This point calls for further investigation; however, there is one interesting hypothesis that aligns with the data. The behaviour of the complete filter is mostly dependant on the angular velocity, while the complementary part of the filter works by correcting the estimation based on attitude deviations. Given that the first could be seen as a derivative of the second, it would make sense that the difference between the second transfer function to the first is similar to the inclusion of an integrator. But still, further analysis is required. For higher frequencies, the magnitude inverts direction decreasing of $20dB/decade$, which would mean the inclusion of two poles that counteract the presence of that lone zero.

Another interesting factor that arises on the purely complementary filter Bode plots is that the relations between the crossed terms seem to be reciprocated. To clarify, one could check the magnitudes of the transfer function between $\hat{\tau}/\kappa_y$ and find the same results when analysing $\hat{\kappa_y}/\tau$. This behaviour was observed in a few different experiments; however, no proof was developed to explain it. This could probably be done by algebraically determining the equations that connect each one and linearizing the equations around an equilibrium point to obtain the transfer functions that generated these graphs.

4.2 Complementary Filter Tuning Comparison

This second simulation batch outcome, shown in Fig. 4, compares the behaviour of two complementary filters, tuned with different sets of gains, that do not consider the rate gyro measurements. The most significant change, due to tuning, is the frequency range the estimator corrective term will let through. From test 2 to test 3, the gains were increased, meaning that a similar error in attitude estimation would cause a more significant correction on test 3 than on test 2. With this change, the estimator shifts its response to higher frequencies.

4.3 Noise Input Effects

This third simulation batch outcome, shown in Fig. 5, analyses the behaviour of the full complementary filter receiving a noisy input. Recall that the bias estimation term is turned off, which is why the Bode plot starts from a static error instead of lower magnitudes. The direct transfer function shows simple behaviour with a roll-off of about $-20dB/decade$, alluding to the presence of a pole on that frequency window. Some of the crossed terms present the phase delay of $-180°$, similarly to what has already been discussed. One phenomenon that requires further analysis is that the crossed terms seem to all end their magnitude plots on a slope of $-30dB/decade$. Since the window of frequencies ends around those values, there is not much information to explain the phenomena. One open hypothesis would be that there is another pole inside the frequency window and that the graph ends right before the curve stabilises in $-40dB/decade$.

5. CONCLUSION

This paper proposes a method for state estimation of beam-like flexible structures for active shape control pur-

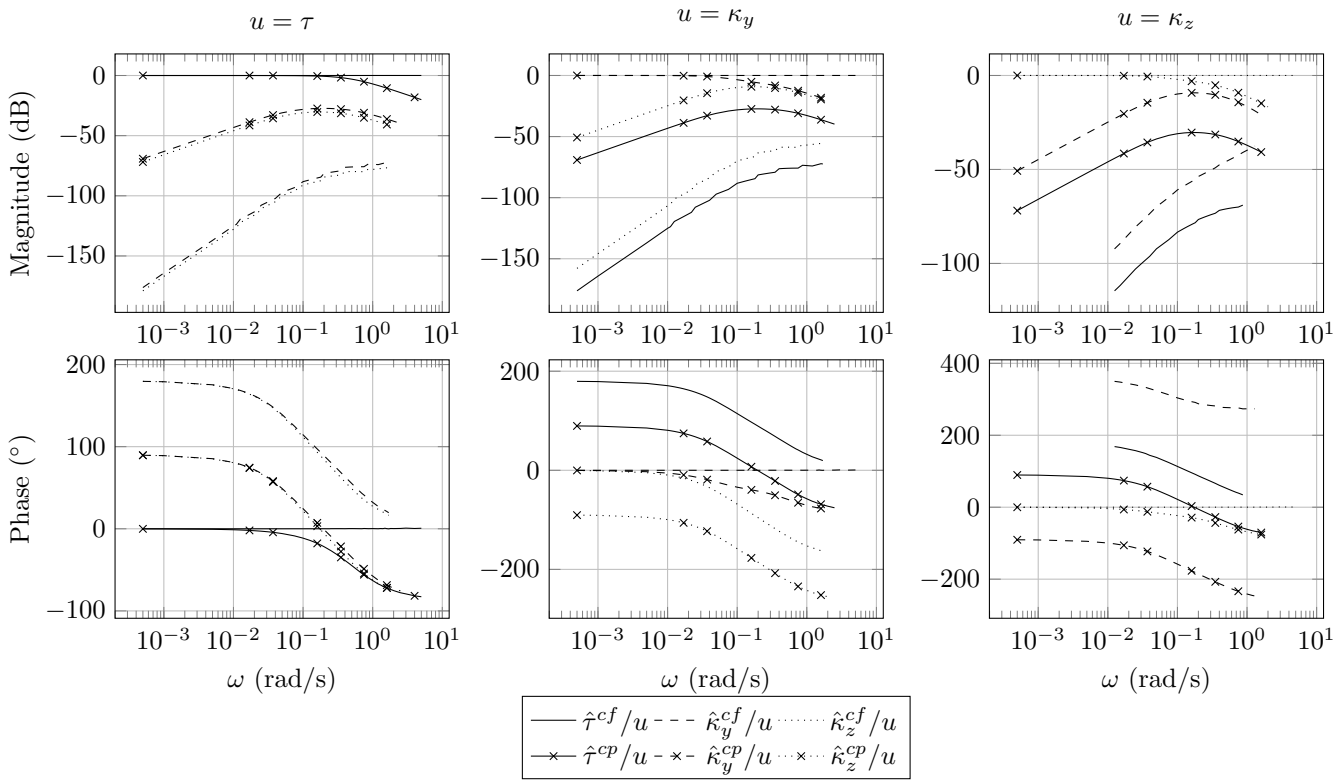

Fig. 3. Bode plots of $\hat{\kappa}_i/u$ where u equals τ (on the left), κ_y (on the center), or κ_z (on the right), comparing the performance of the complete filter (superscript cf) and complementary part only (superscript cp).

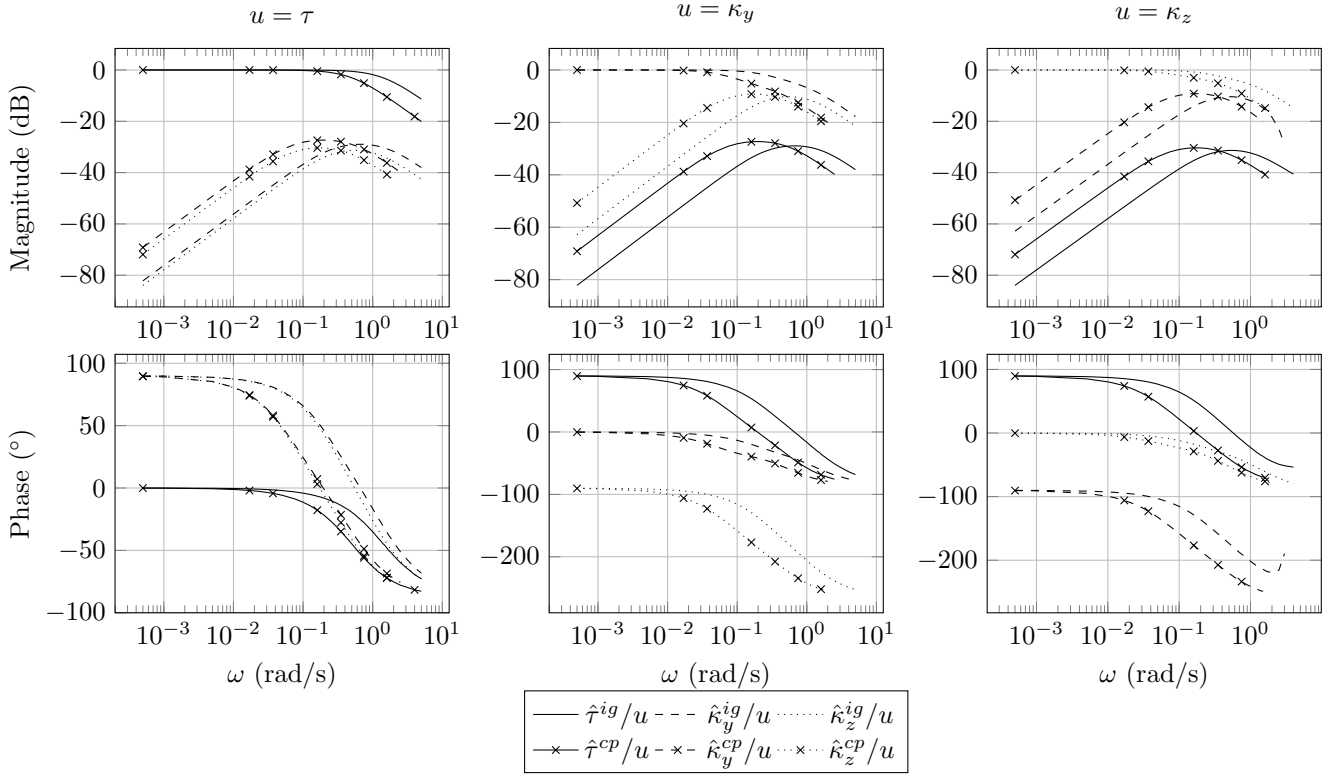

Fig. 4. Bode plots of $\hat{\kappa}_i/u$ where u equals τ (on the left), κ_y (on the center), or κ_z (on the right), comparing the performance of the complementary part with the initial tuning (superscript cp) and complementary part with increased gains (superscript ig).

poses. Initial definitions are presented, and the algorithm is derived along with its application domain and limitations. Further analysis through a frequency sweep experiment is conducted. Admittedly, some behaviours had not been

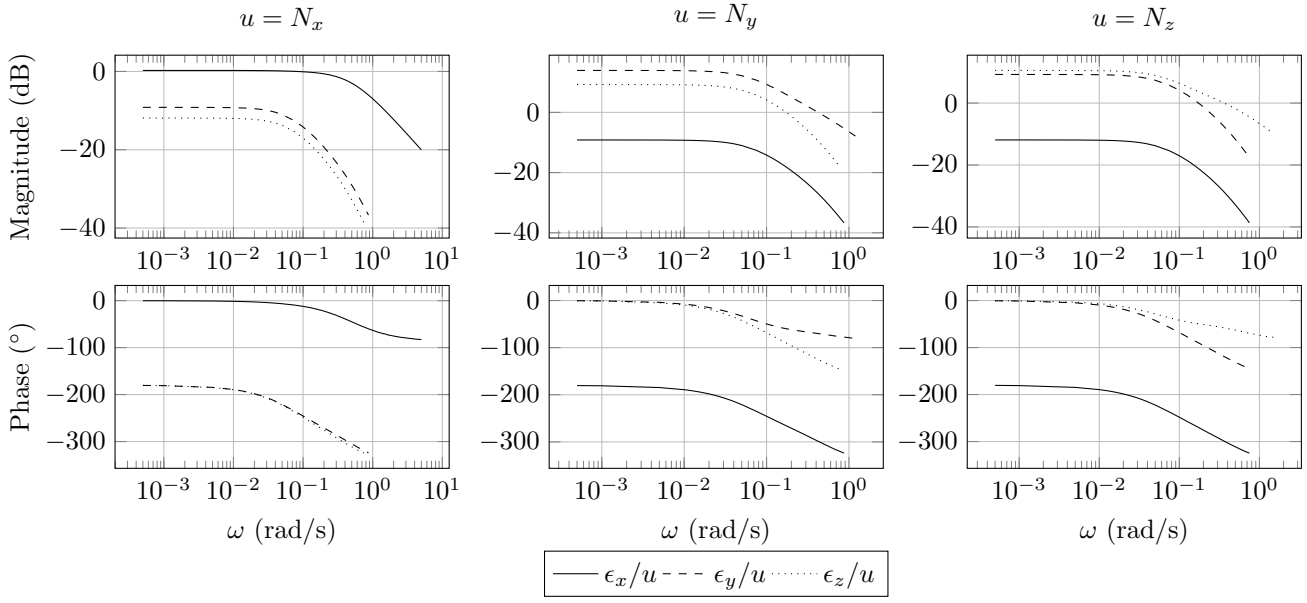

Fig. 5. Bode plots of ϵ_i/u, where $\epsilon_i = \hat{\boldsymbol{K}}_i(t) - \boldsymbol{K}_i$ is the estimated curvature error on each of the axes and u is a noise input of amplitude 10^{-4} rad/s added to gyro measurements on the x-axis (on the left), y-axis (on the center), and z-axis (on the right).

predicted, however, global trends followed the authors' expectations. With the analysis done, the authors expect to use this information in future works to tune the estimator along with a control loop to attempt active shape control with proper loop shape recovery.

Given its dependency on complementary filtering, the estimator partially inherits the filter's stability properties. In this study, only one of the beam edges was free to move, therefore effectively simulating a single filter. However, the *DD0T* method relies on two separate filters. Future work plans to study this stability problem, including having the reference extremity on a non-inertial reference frame. Another perspective is to merge the calculations of the complementary filter along with the estimator.

Finally, given the estimator's software and hardware simplicity, this method could be included with limited intrusion in existing aircraft. Observing the curvature variables along a wing could enable, for instance, the identification of perilous deformed conditions and curvature feedback in active shape controllers, the later being the ultimate goal of this study. Another possible application would be towards large-amplitude ground vehicle testing campaigns, given the method's capacity to measure nonlinear deformations.

REFERENCES

Cesnik, C.E.S. and Brown, E.L. (2003). Active Warping Control of a Joined-Wing Airplane Configuration. *AIAA/ASME/ASCE/AHS/ASC Structures, Structural Dynamics and Materials Conference*, AIAA 2003-1715. doi:10.2514/6.2003-1715.

González, P.J., Cesnik, C.E.S., and Silvestre, F.J. (2018). Implementation and Flight Testing of an Enhanced Stability System for a Very Flexible Aircraft. In *31st Congress of the International Council of the Aeronautical Sciences*.

Lustosa, L.R., Kolmanovsky, I., Cesnik, C.E.S., and Vetrano, F. (2021). Aided Inertial Estimation of Wing Shape. *Journal of Guidance, Control, and Dynamics*, 44(2), 210–219. doi:10.2514/1.G005368.

Mahony, R., Hamel, T., and Pflimlin, J.M. (2008). Nonlinear Complementary Filters on the Special Orthogonal Group. *IEEE Transactions on Automatic Control, Institute of Electrical and Electronics Engineers*, 53(5), 1203–1217. doi:10.1109/TAC.2008.923738.

Meyer, R., Kirmse, T., and Boden, F. (2014). Optical In-Flight Wing Deformation Measurements with the Image Pattern Correlation Technique. *New Results in Numerical and Experimental Fluid Mechanics IX, Notes on Numerical Fluid Mechanics and Multidisciplinary Design*, Springer, 124, 545–553. doi:10.1007/978-3-319-03158-3_55.

Pang, Z.Y. and Cesnik, C.E.S. (2016). Flight Shape Estimation of Very Flexible Unmanned Aerial Vehicle. In *57th AIAA/ASCE/AHS/ASC Structures, Structural Dynamics, and Materials Conference*, AIAA 2016-1955. doi:10.2514/6.2016-1955.

Reis, F.P., Lustosa, L.R., and Poussot-Vassal, C. (2022). Nonlinear Curvature Basis Functions For Strain-Based Geometrically Nonlinear Beams For Very Flexible Aircraft Modeling. In *International Forum on Aeroelasticity and Structural Dynamics*.

Renaud, F., Lo Feudo, S., Dion, J.L., and Goeller, A. (2022). 3D Vibrations Reconstruction with Only One Camera. *Mechanical Systems and Signal Processing*, 162, 108032. doi:10.1016/j.ymssp.2021.108032.

Zhang, D., Zheng, X., Xie, Y., and Hu, X. (2022). Angular-Accelerometer-Based Flexible-State Estimation and Tracking Controller Design for Hypersonic Flight Vehicle. *Aerospace*, 9(4). doi:10.3390/aerospace9040206.